

Moiré metrology of energy landscapes in van der Waals heterostructures

Dorri Halbertal^{1*}, Nathan R. Finney², Sai S. Sunku¹, Alexander Kerelsky¹, Carmen Rubio-Verdú¹, Sara Shabani¹, Lede Xian³, Stephen Carr⁴, Shaowen Chen¹, Charles Zhang¹, Lei Wang¹, Derick Gonzalez-Acevedo¹, Alexander S. McLeod¹, Daniel Rhodes¹, Kenji Watanabe⁵, Takashi Taniguchi⁴, Efthimios Kaxiras^{3,6}, Cory R. Dean¹, James C. Hone², Abhay N. Pasupathy¹, Dante M. Kennes⁷, Angel Rubio^{3,8}, D. N. Basov¹

The emerging field of twistronics, which harnesses the twist angle between layers of two-dimensional materials, has revolutionized quantum materials research^{1,2}. The twist between the layers creates a moiré superlattice, a large-scale periodic modulation, with dramatic impact on properties of two-dimensional systems. This approach offers the novel means to control topology and strong correlations – topics of great interest in contemporary quantum physics^{1–33}. At the small twist limit, and particularly under strain, as atomic relaxation becomes prevalent the emergent moiré superlattice encodes elusive insights into the local interaction between the layers. Here we introduce moiré metrology as an experiment-theory codesign framework to probe the stacking energy landscape of bilayer structures at the 0.1 meV/atom scale, outperforming the gold-standard of quantum chemistry^{34,35}. We study the shapes of moiré domains and their boundaries, as visualized with numerous nano-imaging techniques. We compare these experimental maps with real-space atomic relaxation simulations, and through this process assess and refine models for the interlayer interaction. We document the prowess of moiré metrology for three representative systems: twisted bilayer graphene, twisted double bilayer graphene and twisted H-stacked MoSe₂/WSe₂. Moiré metrology establishes sought after experimental benchmarks³⁶ for binding and exfoliation energies and improves account of the stacking energy function, thus enabling accurate modelling of twisted multilayers.

Twisted van der Waals structures, such as twisted bilayer graphene^{3–20} (TBG), twisted double bilayer graphene^{21–23} (TDBG) and twisted transition-metal-dichalcogenides^{24–28} are in the vanguard of quantum materials research^{1,2}. The twist between the layers leads to large-scale periodic perturbations of stacking configurations, called a moiré superlattice. Because atomic layers in van der Waals (vdW) materials are not rigid but instead behave as deformable membranes, moiré superlattices acquire additional attributes. As two atomic layers with a small relative twist angle come in contact, the atomic positions relax to minimize the total energy. Through the relaxation process domains of lowest energy configurations form and become separated by domain walls of transitional configurations^{37–39} (Fig. 1a). The generalized stacking fault energy function (GSFE), which provides the energetic variations across different stacking configurations, is the fundamental property that describes relaxed vdW interfaces^{37,40}.

¹Department of Physics, Columbia University, New York, NY, USA.

²Department of Mechanical Engineering, Columbia University, New York, NY, USA.

³Max Planck Institute for the Structure and Dynamics of Matter and Center Free-Electron Laser Science, Luruper Chaussee 149, 22761 Hamburg, Germany.

⁴Department of Physics, Harvard University, Cambridge, Massachusetts 02138, USA.

⁵National Institute for Material Science, Tsukuba, Japan

⁶John A. Paulson School of Engineering and Applied Sciences, Harvard University, Cambridge, Massachusetts 02138, USA.

⁷Institut für Theorie der Statistischen Physik, RWTH Aachen University, 52056 Aachen, Germany.

⁸Center for Computational Quantum Physics, Flatiron Institute, New York, NY 10010 USA.

The GSFE is commonly calculated using density functional theory (DFT)^{37,40}. Experimental techniques⁴¹ to probe the GSFE are currently restricted to the stable lowest energy configuration, and are very limited in energy resolution compared to the variability among theoretical descriptions. Here we show that the GSFE is encoded in fine details of the relaxed moiré super-lattice patterns at the low twist-angle limit. In particular, the shape of domains and domain walls networks, as well as domain wall width, abide by transitional configurations beyond the lowest-energy stackings of the domains. More specifically, we distinguish between single and double domain walls (SDW and DDW). SDWs separate two distinct stacking configurations of a moiré superlattice (for instance, ABAB [MM'] and ABAB [MX'] in the TDBG [for twisted H-stacked MoSe₂/WSe₂, or T-H-MoSe₂/WSe₂ for short] example of Fig. 1a). DDWs, formed from

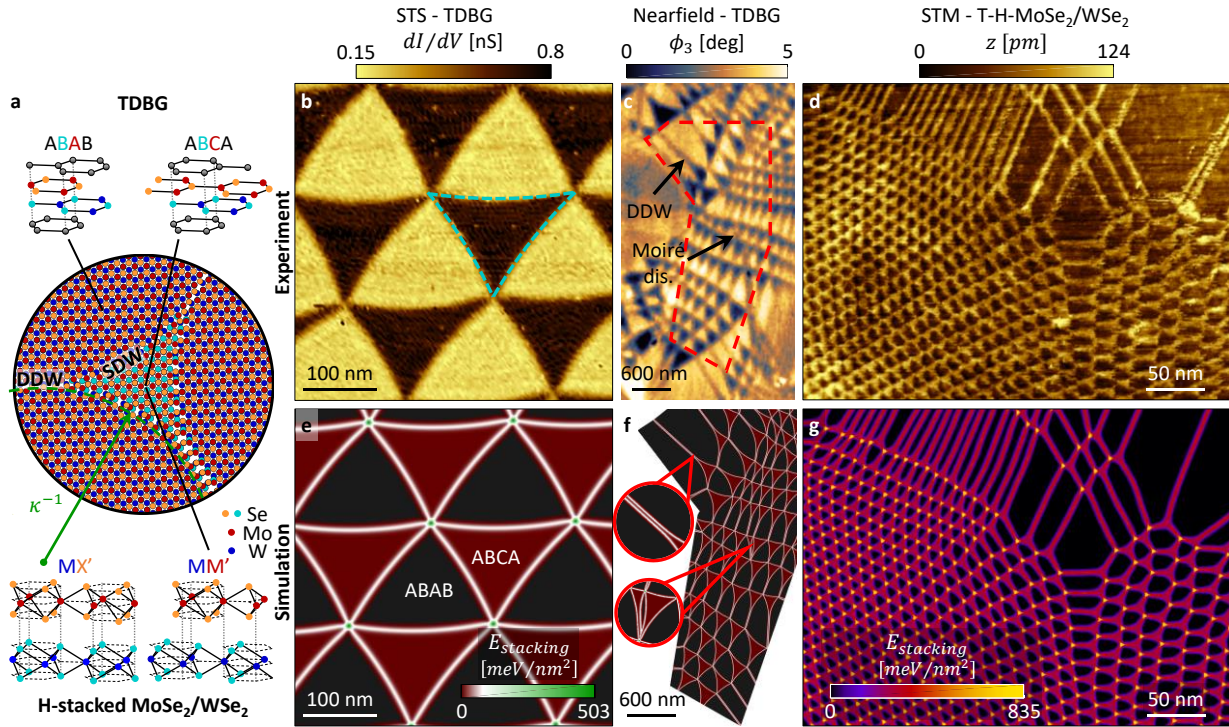


Figure 1 | Physics of atomic layers stacking probed by moiré metrology in vdW twisted bilayers – experiment and theory. **a**, Illustration of domain formations in a relaxed twisted bilayer structure. Center: atomic positioning after relaxation (see SI S1 for more details) for twisted double bilayer graphene (TDBG). Atoms are colored to highlight stacking configurations. The energy imbalance leads to curved single domain walls (SDW), with radius indicated by κ^{-1} , and in some cases with formation of double domain walls (DDWs). Two systems with energy imbalance are considered: TDBG (top) and T-H-MoSe₂/WSe₂ (bottom). **b**, STS map of TDBG with $\theta = 0.07^\circ$, revealing rhombohedral (ABCA – dark) and Bernal (ABAB – bright) domains with minimal external strain. The rhombohedral phase bends inward (dashed turquoise line) revealing an energy imbalance between the two phases as discussed in the text. **c**, Mid-IR (940 cm^{-1}) nearfield phase imaging of TDBG resolves ABCA (dark) and ABAB (bright) phases and DDW formations. **d**, STM topography map of T-H-MoSe₂/WSe₂ resolving MM' (bright) and MX' (dark) stacking configurations as well as DDW formation in various strain conditions. **e-g**, Stacking energy density from full relaxation calculations of the experimental cases of **b-d** respectively (see methods, SI sections S1-2 and text for more details). The color-map is shared for **e-f**. Magnified regions in **f** (and arrows in **c**) highlight a DDW formation and a moiré dislocation (see discussion in SI S3). Calculated region of **f** is marked by dashed shape in **c**.

the collapse of two SDWs, separate identical phases (ABAB for TDBG and MX' for T-H-MoSe₂/WSe₂ in Fig. 1a). The formation and nature of DDWs result from attraction of SDWs as they are brought together (for instance, due to external or relaxation induced strain), and is proven here to provide a reliable read-out of the underlying energetics. In cases of inequivalent two lowest energy configurations (as in Fig. 1), the SDW develops a finite curvature κ , allowing one to extract the domains energy imbalance with an accuracy outperforming the $\sim 3 \text{ meV}/\text{atom}$ of the gold standard of quantum chemistry^{34,35}.

Moiré metrology, presented here, correlates measurable spatial patterns of the relaxed moiré superlattice (such as shapes of domains, SDWs and formation of DDWs) with modelling based on the GSFE. To do so we developed a continuous two dimensional relaxation simulation. The model searches for local inter-layer displacement fields that minimize the total energy of the multilayer, as a sum of elastic and stacking energy terms (see SI sections S1-2 for more details, also see Ref. 39 for an alternative approach). The equations are solved in real space and thus capture subtle experimental details that remained underexplored. Fig. 1b-g is a tour-de-force of moiré metrology combining experimental imaging of different systems, techniques and length-scales (Fig. 1b-d), and their respective modelling (Fig. 1e-g). Fig. 1b-d were acquired with modern scanning probe microscopy (SPM) techniques: scanning tunneling microscopy and spectroscopy²¹ (STM and STS) and mid-infrared range (mid-IR) scanning nearfield optical microscopy¹² (SNOM). These techniques resolve stacking configurations based on local topographic (STM), electronic (STS) and mid-IR optical conductivity (mid-IR SNOM) contrasts. In low strain TDBG, the model (Fig. 1e) captures the fine curving of SDWs (Fig. 1b). In cases of higher strain (Fig. 1c and modelling in Fig. 1f) we observe the formation of one dimensional DDW structures (inset of Fig. 1f highlights an example). Similarly, DDW formations and SDW curving were observed (Fig. 1d) and modelled (Fig. 1g) in T-H-MoSe₂/WSe₂, with excellent agreement across different length-scales of the image (see SI S3 for additional analysis). Next we will illustrate in detail how moiré super-lattices reveal the energy landscape information using TBG and TDBG as prototypical examples.

To study the energy landscape of TBG, we focus on the interplay between SDW and DDW formations. Fig. 2a presents a non-local nano-photocurrent map of TBG in the minimal twist limit $< 0.1^\circ$. Bright spots in the photo-current map highlight the AA sites (indicating higher absorption – see methods and SI S4). The AA sites are connected by domain walls separating AB and BA domains. The resultant moiré super-lattice is clearly affected by strain, inferred from the distorted triangular pattern, especially near the edges of the stack. There, we observe the merging of two SDWs into a single DDW (selected locations are marked in Fig. 2a). We successfully account for the observed network within a model addressing a competition between SDWs and DDWs. To grasp the essential physics, we first assume a characteristic energy of forming a segment of DDW and SDW. We define a dimensionless domain-wall formation ratio as the ratio of DDW and SDW line energies, $\bar{\beta} = \gamma_{DDW}/\gamma_{SDW}$. In addition to $\bar{\beta}$, the model input includes the AA sites of the moiré pattern as the fixed vertices of the triangles forming the network. We explore the SDW vs. DDW structures that emerge for a given value of the single tuning parameter $\bar{\beta}$. The case of $\bar{\beta} = 2$ implies there is no benefit in forming a DDW, and the optimal structure would simply be straight SDWs connecting the AA sites. For $\bar{\beta} < 2$ the two SDWs attract each other favoring the emergence of DDW segments (see SI S4 and Supplementary Video 1 for details). Our modeling captures the overall shape of the experimental map for $\bar{\beta} = 1.90$ (Fig. 2a) The agreement is remarkable considering the minimal modeling we employ. We conclude that in order for a TBG model to reproduce the experimental picture, two SDWs have to sufficiently attract one another as quantified by the fitted $\bar{\beta}$. In that sense, as we show more rigorously below, moiré metrology puts constraints the GSFE.

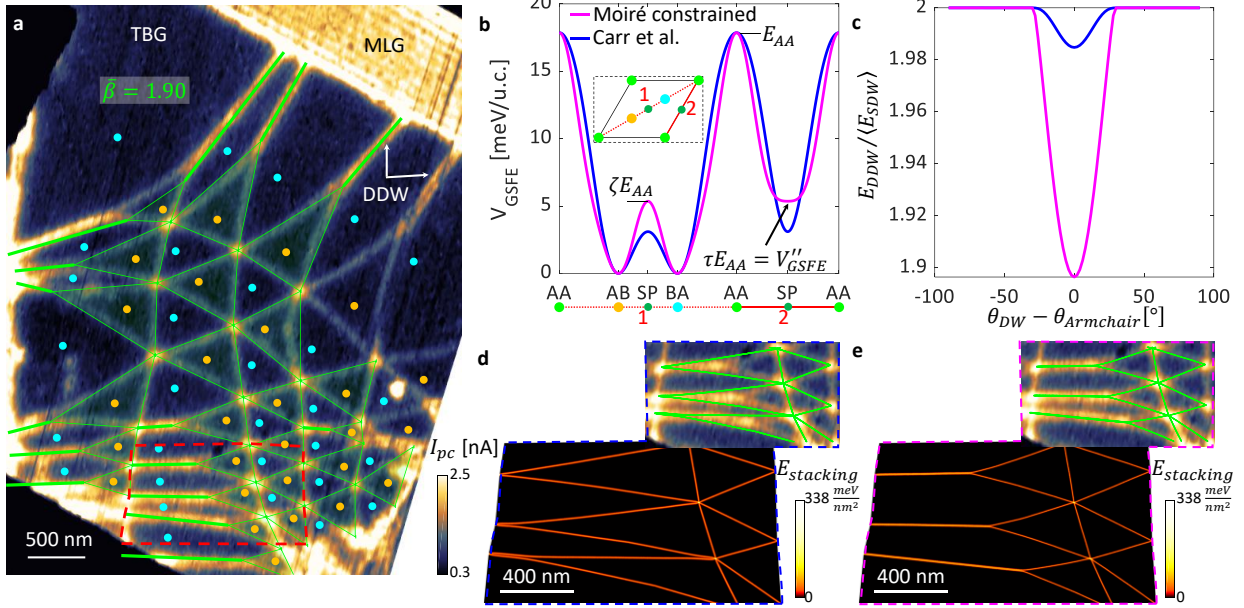


Figure 2 | Energy landscape of twisted bilayer graphene (TBG) revealed by the interplay between double (DDW) and single (SDW) domain walls. **a**, Non-local nano-photocurrent map of moiré superlattice of a TBG sample at the minimal twist limit (see methods for more details). The technique reveals the formation of DDWs (marked by “DDW”) at strained domains, separating domains of identical stacking configurations (each configuration is indicated by dots of a given color [AB – orange, BA - cyan]). The green network overlaid on the data corresponds to the prediction by a single tuning parameter model (see text and SI S6). **b**, GSFE of TBG from Ref. 37 (blue) and a moiré constrained version (magenta). The unit-less parameters ζ , τ , spanning the phase space of GSFE candidates for TBG, are illustrated (see SI S6). Inset: path in configuration space for presented GSFE line-cuts. **c**, Effective attraction between SDWs as reflected by DDW to SDW energy ratios for different SDW orientations (relative to armchair direction) for both models. E_{DDW} is the DDW line-energy for a DDW along the armchair direction and similarly $\langle E_{SDW} \rangle$ is for the average of the two SDWs comprising the DDW. **d-e**, Stacking energy density from 2D relaxation calculation (see methods and SI S2) for the two discussed GSFE choices (**d** – literature, **e** – moiré constrained version with $\tau = 0.025, \zeta = 0.3$) showing fundamental differences in formation of DDWs. Inset: extracted domain wall structures from relaxation calculations overlaid on experimental results.

To quantify how the observed moiré networks constrain the stacking energy landscape, we span all realistic GSFE’s satisfying the symmetry of TBG over a 2D unit-less parameter space (ζ , τ) (as illustrated in Fig. 2b and discussed at SI S4), such that each point on the (ζ , τ) plane represents one GSFE candidate. We solve a set of 1D relaxation problems describing the profiles of SDWs and DDWs (see SI S1 for more details on relaxation codes), and extract the domain wall formation ratio $\bar{\beta}$. This allows us to define a band in (ζ , τ) plane of GSFE’s that comply with the experimental $\bar{\beta} = 1.90$ (see SI Fig. S3g). Fig. 2b compares one GSFE moiré constrained candidate with the $\bar{\beta} = 1.90$ band (magenta) with the well-accepted choice of GSFE of Ref. 37 (blue), which notably falls outside of the band with $\bar{\beta} = 1.98$. The moiré metrology analysis indicates that SDWs implied by GSFE in Ref. 37 insufficiently attract one another (blue curve in Fig. 2c) to account for the observed network, as indeed revealed in Fig. 2d. In contrast, the moiré-constrained candidate (magenta in Fig. 2b) with a flatter saddle point promotes stronger SDWs attraction

across a broad range of domain wall orientations (magenta curve in Fig. 2c; see SI sections S1 and S5 for additional details), and yields excellent agreement with the data (Fig. 2e). Regardless of the good agreement, the relatively flat saddle point comes as a surprise, and may in fact correct for an unknown effect unrelated to interlayer energy.

Compared to TBG, the TDBG system makes an even more interesting case-study due to the small yet finite imbalance between the two lowest energy phases: Bernal (ABAB) and rhombohedral (ABCA) stackings²¹. This imbalance results in an energy cost per-unit-area (σ) for rhombohedral relative to Bernal stackings, leading to characteristic curved domains^{21,29} (see Fig. 1a-b). Exploring large areas of TDBG reveals a rich distribution of rhombohedral domain shapes (see Fig. 1c and other TDBG images in this work). Figure 3a summarizes this distribution as a histogram of inverse curvature values (κ^{-1}), extracted from images as in Fig 1b (see SI section S6 for more examples). The histogram reveals a distinct clustering about a value of $\kappa^{-1} = 440 \pm 120 \text{ nm}$, which we use to assess the accuracy of several variants of the GSFE from available DFT functionals (Fig. 3b and see methods). All reported GSFE variants are qualitatively similar to the TBG case, peaking at the BAAC configuration, and having a saddle point barrier between ABAB and ABCA. A closer inspection (inset) reveals a profound difference between the GSFEs for the ABCA relative to the ABAB that governs domain curvature. We model the domain curvature and structure by a continuous 2D relaxation code (SI section S1). Figs. 3c-d show two representative cases, with disparate outcomes. In Fig. 3c (resembling the experimental case of Fig. 1b) the energy is minimized by slight bending of the SDW into the ABCA region. As the twist angle decreases (or as strain increases as in Fig. 1c), at some point it becomes energetically beneficial to form DDWs (Fig. 3d). As the twist angle further decreases, the shape of the ABCA domains remains unchanged. Similarly, solving for the domain formation for all DFT approaches and across a wide twist angle range we compare the extracted κ^{-1} . Interestingly, κ is independent of the twist angle for all GSFE variants (with values indicated by colored lines over Fig. 3a), which is not generally the case (see discussion in SI S7). The domain structures are further captured by the 2D “soap-bubble” model, as seen in turquoise dashed lines in the representative cases of Fig. 3c-d and more generally in Supplementary Videos 2-5. This model approximates the total energy as a sum of a domain area term and two line-energy terms as $E = \int_{SDW} dl \gamma_1(\varphi) + \int_{DDW} dl \gamma_2(\varphi) + \sigma S$, where $\gamma_{1,2}$ are the line-energies of SDW and DDW as a function of the domain-wall orientation respectively, the integrations are along the domain walls, and S is the area of the domain (see SI section S7). All model parameters require only the GSFE (and elastic properties) to describe domain shapes, with no additional tuning parameters (SI section S7). One approach, DFT-D2, remarkably reproduces the experimental cluster (Fig. 3a), due to relatively high σ and comparable line-energies to other approaches (see SI S2).

The rhombohedral domains represented in the histogram of Fig. 3a exemplify well-defined electrostatic environment near charge neutrality point (CNP) in the absence of the interlayer bias. As shown recently²⁹, upon charging and biasing the balance between the rhombohedral and Bernal phases can shift. An extreme demonstration of malleability of TDBG moiré patterns under a non-uniform distribution of charges and high strain conditions is presented in Fig. 3e. 3 holes (marked by blue circles) punctured one of the bilayers. This procedure prompts a highly strained moiré pattern, most strongly manifested in the densely packed parallel DDWs structures connecting the two bottom holes. The stack shows strong defect-induced doping (see discussion in SI S5), apparent in the enhanced nearfield contrast

between the ABCA (dark) and ABAB (bright) phases (compare to contrast of Fig. 1c). Further support for the high non-uniformity of charge distribution is an observed region of flipped balance, where the ABAB phase becomes unstable relative to ABCA across a sharp (~ 50 nm) interface (to the left of the top hole). Attempting to model the moiré superlattice with the DFT-D2 GSFE at CNP (red in Fig. 3b) fails to capture

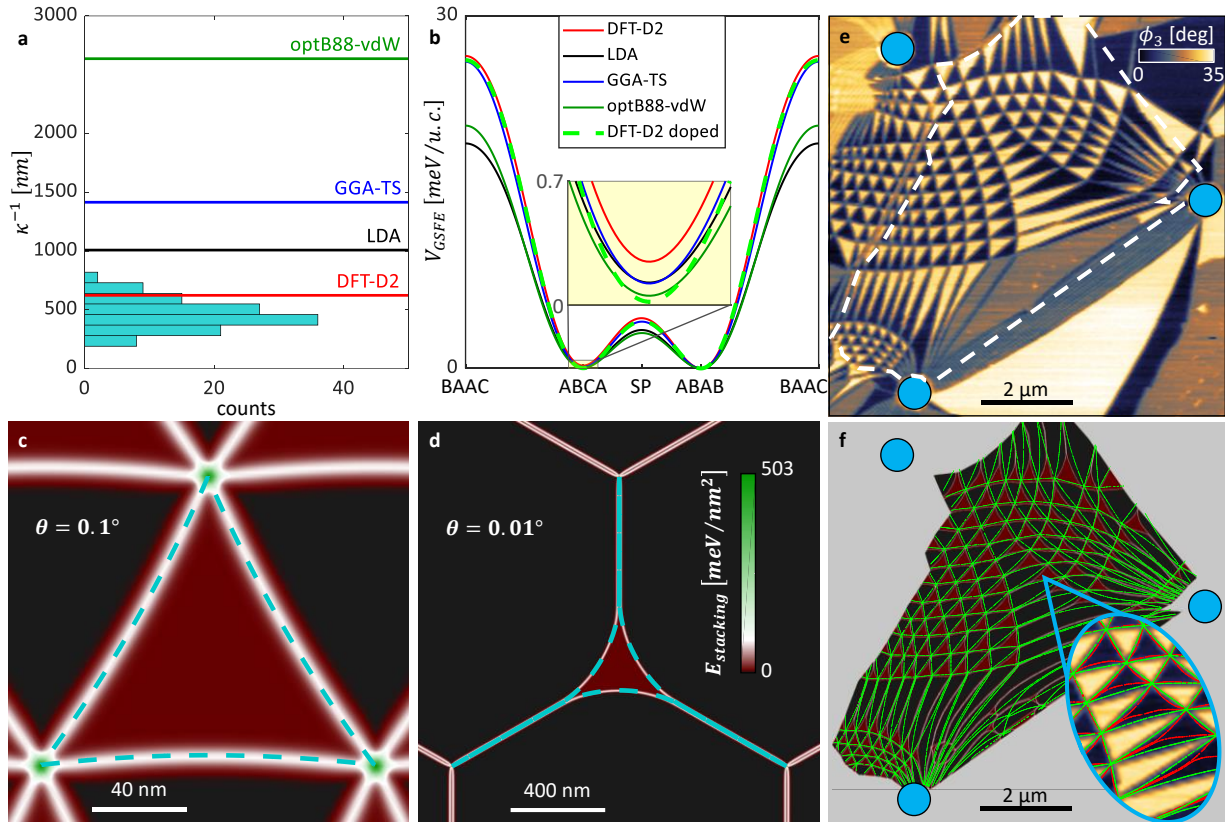


Figure 3 | Moiré super-lattice study of rhombohedral domains in twisted double bilayer graphene (TDBG). **a**, Curvature histogram across all measured domains near charge neutrality point (see discussion in SI S7), showing a clear cluster at 440 ± 120 nm. Calculated curvatures of 4 DFT approaches (of **b**) are illustrated over the histogram (colored horizontal lines). **b**, GSFE of TDBG based on 4 different approaches (solid lines, see methods). The dashed light-green line is the GSFE for DFT-D2 approach at a doping level of $8 \cdot 10^{12} \text{ cm}^{-2}$. Inset: enlarged view highlighting small difference between ABCA and ABAB configurations ($V_{GSFE}(ABAB) = 0$ identically). **c-d**, Mechanical relaxation solutions (false-color: stacking energy density) and “soap-bubble” model domain shape (dashed turquoise) for 2 representative twist angles (**c**: 0.1° , **d**: 0.01°) for DFT-D2. **e**, Mid-IR (940 cm^{-1}) nearfield phase imaging of a defect-induced doped TDBG (see SI S7). 3 holes punctured one of the bilayers (blue circles - see methods) and induce a non-trivial external strain map. Mid-IR imaging resolves ABCA (dark) and ABAB (bright) phases and double-domain wall (DDW) formations (for instance, the multiple-DDW formation connecting bottom holes). **f**, Comparing relaxation calculations solutions of un-doped vs. $8 \cdot 10^{12} \text{ cm}^{-2}$ doped DFT-D2 approach GSFE, simulating the experimental case (marked by dashed shape in **e**). False-color represents stacking energy density of un-doped case, overlaid (green dots) with tracked domain walls in the doped case. Inset: Highlighting differences between model by overlaying domain wall formation of doped (red) and un-doped (green) cases over strained region in the experimental map. The color-map is shared for **c-e**.

the observed structure of excessively curved SDWs (color-map of Fig. 3f). However, when introducing a doping level of $8 \cdot 10^{12} \text{ cm}^{-2}$ the resulting GSFE (dashed light-green in Fig. 3b) better captures the observed structure (green dots in Fig. 3f tracking the domain walls in the calculation). The difference between the two models becomes more pronounced for regions of higher strain, as highlighted in the inset of Fig. 3f (compare green and red dots in respect to the experimental map). Therefore, minuscule energy differences between models of order $0.1 \text{ meV}/u. c.$ (inset of Fig. 3b) result in measurable spatial features of the relaxed moiré patterns. To put this figure in context, the theoretical method which is widely considered as the gold-standard of ab-initio quantum chemistry^{34,35} yields an accuracy as low as $3 \text{ meV}/atom$ ³⁵.

To understand the enhanced sensitivity of moiré metrology under strain (as seen in fig. 3F), we propose an alternative description of the moiré superlattice in terms of geometric interference pattern of the lattices of the two layers (see SI section S1). At minute twist angles, the relaxed moiré patterns are essentially a projection of the detailed energy landscape over space, accumulated over large regions compared to the atomic scale. The introduction of strain between the layers, whether naturally occurring or externally controlled, alters the interference pattern (SI section S8). As strain pushes the domain walls in Figs. 1-3 together, it also promotes their interaction; both effects are reflected in the relaxed moiré pattern (also see Supplementary Video 6).

Moiré metrology, introduced here, correlates first principle calculations of the stacking energy function with measurable spatial features of twisted vdW systems. The stacking energy function is widely used for modelling twisted multilayers across a broad range of twist angles and strain conditions, and has direct implications for the electronic band-structure⁴². Therefore, by providing a reliable account of the stacking energy function, moiré metrology has a broad impact across the field of vdW heterostructures. Furthermore, the moiré metrology tools can also be used for modelling and designing non-uniform strain fields in realistic devices. Finally, due to its outstanding stacking energy sensitivity, we propose moiré metrology as a concrete experimental path to provide much needed benchmarks for first-principle theoretical approaches³⁶.

References

1. Balents, L., Dean, C. R., Efetov, D. K. & Young, A. F. moiré flat bands. *Nat. Phys.* (2020). doi:10.1038/s41567-020-0906-9
2. Yankowitz, M., Ma, Q., Jarillo-Herrero, P. & LeRoy, B. J. van der Waals heterostructures combining graphene and hexagonal boron nitride. *Nat. Rev. Phys.* **1**, 112–125 (2019).
3. Hesp, N. C. H. *et al.* Collective excitations in twisted bilayer graphene close to the magic angle. *arXiv Prepr.* **1910.07893**, (2019).
4. Huang, S. *et al.* Topologically Protected Helical States in Minimally Twisted Bilayer Graphene. *Phys. Rev. Lett.* **121**, 37702 (2018).
5. Kim, K. *et al.* Tunable moiré bands and strong correlations in small-twist-angle bilayer graphene. *Proc. Natl. Acad. Sci. U. S. A.* **114**, 3364–3369 (2017).
6. Lopes Dos Santos, J. M. B., Peres, N. M. R. & Castro Neto, A. H. Graphene bilayer with a twist: Electronic structure. *Phys. Rev. Lett.* **99**, 19–22 (2007).

7. Lu, X. *et al.* Superconductors, orbital magnets and correlated states in magic-angle bilayer graphene. *Nature* **574**, 653–657 (2019).
8. Rickhaus, P. *et al.* Transport Through a Network of Topological Channels in Twisted Bilayer Graphene. *Nano Lett.* **18**, 6725–6730 (2018).
9. Alden, J. S. *et al.* Strain solitons and topological defects in bilayer graphene. *Proc. Natl. Acad. Sci.* (2013). doi:10.1073/pnas.1309394110
10. Sharpe, A. L. *et al.* Emergent ferromagnetism near three-quarters filling in twisted bilayer graphene. *Science* **365**, 605–608 (2019).
11. Stepanov, P. *et al.* Untying the insulating and superconducting orders in magic-angle graphene. *Nature* **583**, (2020).
12. Sunku, S. S. *et al.* Photonic crystals for nano-light in moiré graphene superlattices. *Science* **362**, 1153–1156 (2018).
13. Uri, A. *et al.* Mapping the twist-angle disorder and Landau levels in magic-angle graphene. *Nature* **581**, (2020).
14. Xu, S. G. *et al.* Giant oscillations in a triangular network of one-dimensional states in marginally twisted graphene. *Nat. Commun.* **10**, 3–7 (2019).
15. Bistritzer, R. & MacDonald, A. H. Moiré bands in twisted double-layer graphene. *Proc. Natl. Acad. Sci. U. S. A.* **108**, 12233–12237 (2011).
16. Yankowitz, M. *et al.* Tuning superconductivity in twisted bilayer graphene. *Science* **363**, 1059–1064 (2019).
17. Zondiner, U. *et al.* Cascade of phase transitions and Dirac revivals in magic-angle graphene. *Nature* **582**, 203–208 (2020).
18. Cao, Y. *et al.* Correlated insulator behaviour at half-filling in magic-angle graphene superlattices. *Nature* **556**, 80–84 (2018).
19. Cao, Y. *et al.* Unconventional superconductivity in magic-angle graphene superlattices. *Nature* **556**, 43–50 (2018).
20. Choi, Y. *et al.* Electronic correlations in twisted bilayer graphene near the magic angle. *Nat. Phys.* **15**, 1174–1180 (2019).
21. Kerelsky, A. *et al.* Moire-less Correlations in ABCA Graphene. *arXiv Prepr.* **1911.00007**, (2019).
22. Liu, X. *et al.* Spin-polarized Correlated Insulator and Superconductor in Twisted Double Bilayer Graphene. *arXiv Prepr.* **1903.08130**, (2019).
23. Shen, C. *et al.* Correlated states in twisted double bilayer graphene. *Nat. Phys.* **16**, (2020).
24. Rosenberger, M. R. *et al.* Twist Angle-Dependent Atomic Reconstruction and Moiré Patterns in Transition Metal Dichalcogenide Heterostructures. *ACS Nano* (2020). doi:10.1021/acsnano.0c00088
25. Scuri, G. *et al.* Electrically Tunable Valley Dynamics in Twisted WSe₂/WSe₂ Bilayers. *Phys. Rev. Lett.* **124**, 1–8 (2020).

26. Weston, A. *et al.* Atomic reconstruction in twisted bilayers of transition metal dichalcogenides. *Nat. Nanotechnol.* **15**, 592–597 (2020).
27. Wu, F., Lovorn, T., Tutuc, E. & Macdonald, A. H. Hubbard Model Physics in Transition Metal Dichalcogenide Moiré Bands. *Phys. Rev. Lett.* **121**, 26402 (2018).
28. Yu, H., Liu, G. Bin, Tang, J., Xu, X. & Yao, W. Moiré excitons: From programmable quantum emitter arrays to spin-orbit-coupled artificial lattices. *Sci. Adv.* **3**, 1–8 (2017).
29. Li, H. *et al.* Global Control of Stacking-Order Phase Transition by Doping and Electric Field in Few-Layer Graphene. *Nano Lett.* (2020). doi:10.1021/acs.nanolett.9b05092
30. Woods, C. R. *et al.* Commensurate-incommensurate transition in graphene on hexagonal boron nitride. *Nat. Phys.* **10**, 451–456 (2014).
31. Chen, G. *et al.* Evidence of a gate-tunable Mott insulator in a trilayer graphene moiré superlattice. *Nat. Phys.* **15**, 237–241 (2019).
32. Chen, G. *et al.* Signatures of tunable superconductivity in a trilayer graphene moiré superlattice. *Nature* **572**, 215–219 (2019).
33. Hattendorf, S., Georgi, A., Liebmann, M. & Morgenstern, M. Networks of ABA and ABC stacked graphene on mica observed by scanning tunneling microscopy. *Surf. Sci.* **610**, 53–58 (2013).
34. Dykstra, C. E., Frenking, G., Kim, K. S. & Scuseria, G. E. Computing technologies, theories, and algorithms: The making of 40 years and more of theoretical and computational chemistry. *Theory Appl. Comput. Chem.* 1–7 (2005). doi:10.1016/B978-044451719-7/50044-5
35. Neese, F., Atanasov, M., Bistoni, G., Maganas, D. & Ye, S. Chemistry and Quantum Mechanics in 2019: Give Us Insight and Numbers. *J. Am. Chem. Soc.* (2019). doi:10.1021/jacs.8b13313
36. Mata, R. A. & Suhm, M. A. Benchmarking Quantum Chemical Methods: Are We Heading in the Right Direction? *Angew. Chemie - Int. Ed.* **56**, 11011–11018 (2017).
37. Carr, S. *et al.* Relaxation and domain formation in incommensurate two-dimensional heterostructures. *Phys. Rev. B* **98**, 1–7 (2018).
38. Cazeaux, P., Luskin, M. & Massatt, D. Energy Minimization of Two Dimensional Incommensurate Heterostructures. *Arch. Ration. Mech. Anal.* **235**, 1289–1325 (2020).
39. Enaldiev, V. V., Zólyomi, V., Yelgel, C., Magorrian, S. J. & Fal’ko, V. I. Stacking Domains and Dislocation Networks in Marginally Twisted Bilayers of Transition Metal Dichalcogenides. *Phys. Rev. Lett.* **124**, 206101 (2020).
40. Zhou, S., Han, J., Dai, S., Sun, J. & Srolovitz, D. J. Van der Waals bilayer energetics: Generalized stacking-fault energy of graphene, boron nitride, and graphene/boron nitride bilayers. *Phys. Rev. B* **92**, 1–13 (2015).
41. Wang, W. *et al.* Measurement of the cleavage energy of graphite. *Nat. Commun.* **6**, 1–7 (2015).
42. Carr, S., Fang, S., Zhu, Z. & Kaxiras, E. Exact continuum model for low-energy electronic states of twisted bilayer graphene. *Phys. Rev. Res.* **1**, 1–6 (2019).